

Complex central structures suggest complex evolutionary paths for barred S0 galaxies

Bililign T. Dullo^{1,2*}, Cristina Martínez-Lombilla^{1,2} and Johan H. Knapen^{1,2}

¹*Instituto de Astrofísica de Canarias, Vía Láctea S/N, E-38205 La Laguna, Spain*

²*Departamento de Astrofísica, Universidad de La Laguna, E-38206 La Laguna, Spain*

11 October 2018

ABSTRACT

We investigate three barred lenticular galaxies (NGC 2681, NGC 3945 and NGC 4371) which were previously reported to have complex central structures but without a detailed structural analysis of these galaxies’ high-resolution data. We have therefore performed four- to six-component (pseudo-)bulge/disk/bar/ring/point source) decompositions of the composite (*Hubble Space Telescope* plus ground-based) surface brightness profiles. We find that NGC 2681 hosts three bars, while NGC 3945 and NGC 4371 are double- and single-barred galaxies, respectively, in agreement with past isophotal analysis. We find that the bulges in these galaxies are compact, and have Sérsic indices of $n \sim 2.2 - 3.6$ and stellar masses of $M_* \sim 0.28 \times 10^{10} - 1.1 \times 10^{10} M_\odot$. NGC 3945 and NGC 4371 have intermediate-scale ‘pseudo-bulges’ that are well described by a Sérsic model with low $n \lesssim 0.5$ instead of an exponential ($n = 1$) profile as done in the past. We measure emission line fluxes enclosed within 9 different elliptical apertures, finding that NGC 2681 has a LINER-type emission inside $R \sim 3''$, but the emission line due to star formation is significant when aperture size is increased. In contrast, NGC 3945 and NGC 4371 have composite (AGN plus star forming)- and LINER-type emissions inside and outside $R \sim 2''$, respectively. Our findings suggest that the three galaxies have experienced a complex evolutionary path. The bulges appear to be consequences of an earlier violent merging event while subsequent disk formation via gas accretion and bar-driven perturbations may account for the build-up of pseudo-bulges, bars, rings and point sources.

Key words: galaxies: elliptical and lenticular, cD — galaxies: fundamental parameter — galaxies: nuclei — galaxies: photometry — galaxies: structure galaxies: individual. NGC 2681, NGC 3945 and NGC 4371

1 INTRODUCTION

A large fraction ($\sim 70\%$) of local spiral and lenticular (S0) disk galaxies contain non-axisymmetric stellar structures such as bars and spirals on scales of a few kiloparsecs which are believed to impact on the central stellar structures and non-stellar activities of the galaxies themselves (e.g., Athanassoula 1992; Knapen et al. 1995, 2000; Sellwood & Wilkinson 1993; Eskridge et al. 2000; Laine et al. 2002). High-resolution near-infrared and optical imaging of barred disk galaxies has revealed that such distinct small-scale ($\lesssim 1$ kpc) structures can include bulges, nuclear star clusters, nuclear disks and rings, bars, dust disks and spirals (e.g., Kormendy 1982).

Theory predicts that a large-scale stellar bar drives gaseous material into the nuclear regions of the host galaxy.

Shlosman, Frank & Begelman (1989) proposed that double bars (i.e., bars within bars) plus nuclear rings effectively remove angular momentum from the large-scale disk material, allowing for the transfer of gas (and perhaps stars) towards the central supermassive black hole. This bar-driven gas infall and the subsequent gas accumulation was proposed to account for the enhancement of nuclear starburst events and the slow buildup of the ‘pseudo-bulges’ in barred galaxies (e.g., Kormendy 1982; Pfenniger & Friedli 1991; Athanassoula 1992; Martin 1995; Ho et al. 1997a; Kormendy & Kennicutt 2004; Sheth et al. 2005; Athanassoula 2005; Ann & Thakur 2005; Coelho & Gadotti 2011; Ellison et al. 2011). Nuclear stellar bars and/or spirals may also fuel the AGN (e.g., Athanassoula 1992; Knapen et al. 1995, 2005). Such small-scale nested bars are hosted by around one-third of all barred galaxies, without a clear preference for certain morphological types (e.g., Mulchaey & Regan 1997; Knapen et al. 2000; Erwin & Sparke 2002; Laine et al. 2002; Erwin

* bdullo@iac.es

2004). How nested bars are related in detail to central AGN activity remains, however, largely unclear (e.g., Ho et al. 1997a; Oh et al. 2012; Cisternas et al. 2015). We plan to use detailed analysis of the light distribution of nested bar galaxies, in combination with radio and optical data on their star formation, kinematical, and AGN properties, and in comparison with dynamical modelling, to shed further light on these questions. In this paper we present an initial step: an analysis of the central structures in three barred lenticular galaxies (with one, two, and three bars, respectively).

Early observational works on bar detections and multi-component structural analysis of barred galaxies were done primarily through, first, visual inspection and, later, isophotal analysis of optical and near-infrared galaxy images (e.g., de Vaucouleurs 1974; Scoville et al. 1988; Buta & Crocker 1993; Knapen et al. 1995, 2000, 2002; Shaw et al. 1995; Friedli et al. 1996; Jungwiert, Combes, & Axon 1997; Erwin & Sparke 1999; Laine et al. 2002). Using the IRAF task ELLIPSE to fit the galaxy isophotes, Erwin & Sparke (1999) drew attention to three intriguing barred S0 galaxies, NGC 2681, NGC 3945 and NGC 4371, which have complex central structures and studied here (see also Laurikainen et al. 2010). NGC 3945 and NGC 4371 were previously alleged to be triple-bar galaxies by Wozniak et al. (1995). Erwin & Sparke (1999) noted that NGC 2681 is a triple-bar galaxy and they argued that NGC 3945 and NGC 4371 have a double-bar+nuclear disk+nuclear ring and bar+inner ring structure, respectively (see Laurikainen et al. 2005; 2010). Measuring the stellar rotation and velocity dispersion, Kormendy (1982) had found that the ‘bulges’ of NGC 3945 and NGC 4371 had the highest ratio of rotation velocity to velocity dispersion ($V_{\max}/\sigma = 1.21$) in his sample of nine barred S0 galaxies. The Palomar Survey (Ho et al. 1997b) classified NGC 2681 and NGC 3945 as weakly active LINERs, whereas the nuclear activity of NGC 4371 is very weak.

The central and global structural parameters of NGC 2681, NGC 3945 and NGC 4371 have previously been determined by fitting Sérsic and Nuker models to their surface brightness profiles (e.g., Cappellari et al. 2001; Erwin et al. 2003; Moiseev et al. 2004; Lauer et al. 2005; Ferrarese et al. 2006; Fisher & Drory 2008; Richings et al. 2011; Krajnović et al. 2013; Erwin et al. 2015). However, there were two limitations. First, these works fit a two-component (bulge+disk) model and excluded additional nuclear components (e.g., bars, star clusters and rings). Second, some of these fits are using radially limited ($R \lesssim 20''$) profiles (Lauer et al. 2005; Richings et al. 2011; Krajnović et al. 2013). In contrast, Laurikainen et al. (2010) and Gadotti et al. (2015) fitted a multi-component (bulge+disk+bar+lens) model to extended ($R \gtrsim 100''$) ground-based light profiles with sub-arcsec resolution. Physically motivated multi-component decompositions into bulge, disk, bar, lens, and point-source using high-resolution profiles are important if we are to understand properly the different formation physics that builds up these very distinct components (e.g., Laurikainen et al. 2010; Dullo & Graham 2013, 2014).

We advance such decomposition by extracting composite high-resolution *Hubble Space Telescope* *HST* plus ground-based SDSS light profiles of NGC 2681, NGC 3945 and NGC 4371 that typically span $R \sim 300''$. Section 2.1 de-

Table 1. The galaxy sample

Galaxy	Type	B_T (mag)	D (Mpc)	σ (km s^{-1})	AGN
(1)	(2)	(3)	(4)	(5)	(6)
NGC 2681	(RL)SAB(rs)0/a	11.2	16.8	121	L1.9
NGC 3945	(R)SB(rs)0 ⁺	11.7	19.4	182	L2
NGC 4371	(L)SB _a (r,bl,nr)0 ⁺	11.9	17.3	128	very weak

Notes.—Col. 1: galaxy name. Col. 2: morphological type for NGC 2681 and NGC 4371 are from Buta et al. (2015) and the classification for NGC 3945 is from the NASA/IPAC Extragalactic Database (NED; <http://nedwww.ipac.caltech.edu>). Col. 3: Total B -band magnitude from HyperLeda (<http://leda.univ-lyon1.fr>; Paturel et al. 2003). Note that we did not correct these magnitudes for dust extinction and inclinations. Col. 4: distances are from Tonry et al. (2001) after adopting the correction in Blakeslee et al. (2002). Col. 5: central velocity dispersion from HyperLeda. Col. 6: AGN types are from Ho et al. (1997b) except for NGC 4371 where the classification is from Ho et al. (1995).

scribes the data reduction steps and light profile extraction techniques for these broad-band data. A detailed information on the derivation of colors and mass-to-light ratios for the three galaxies is given in Section 2.1.4. New narrow-band observations, continuum subtraction and flux calibration are discussed in Section 2.2. In this paper, for the first time, we fit four to six-component models to our composite profiles of NGC 2681, NGC 3945 and NGC 4371. Section 3 details these sophisticated multicomponent light profile decompositions, plus our isophotal and fitting analyses, along with a literature comparison. We construct standard emission line diagnostic diagrams using our measurements of the $H\beta$ $\lambda 4881$, $[O \text{ III}] \lambda 5032$, $H\alpha$ $\lambda 6589$, $[N \text{ II}] \lambda 6613$, and $[S \text{ II}] \lambda \lambda 6745, 6757$ line fluxes in the nuclear and circumnuclear regions of these galaxies (Section 4). This enables us to discriminate between nuclear line emission created by starburst events, an AGN or both. Section 5.1 illustrates the importance of global multi-component decompositions by focussing on the fractional luminosities and stellar masses of the bulge and pseudo-bulge components. The role of bars in galaxy structure formation/evolution and their connection to the central AGN activities, along with the origin of our S0 galaxies are discussed in Section 5.2. Section 6 summarises our primary conclusions.

2 DATA

2.1 Broad-band imaging

2.1.1 *HST* images

High-resolution *HST* optical images of NGC 2681, NGC 3945 and NGC 4371 were retrieved from the public Hubble Legacy Archive (HLA)¹. In order to reduce the effects of dust contamination we used images taken through the ACS F814W (similar to the Johnson-Cousins broadband I ; Proposal ID 9788, PI: L. Ho), WFPC2 F814W (\sim broadband I ; Proposal ID 6633, PI: C. Carollo), and ACS F850LP (roughly SDSS- z band; Proposal ID 9401, P. Côté) filters,

¹ <http://hla.stsci.edu>

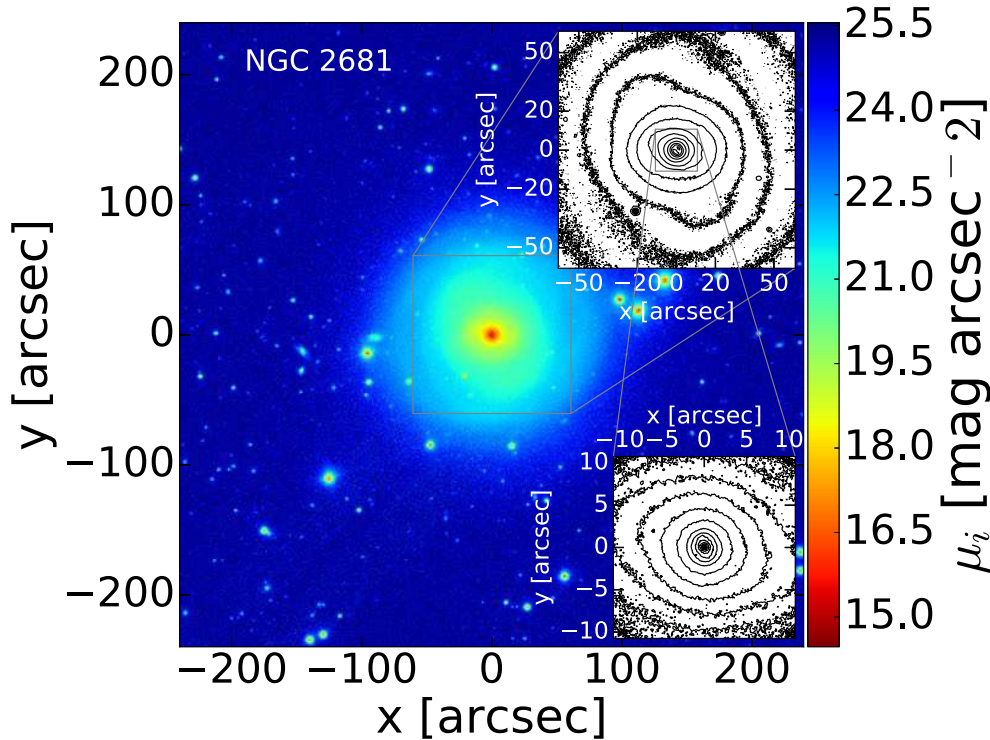


Figure 1. SDSS i -band image of NGC 2681. The top inset shows the surface brightness contours of the SDSS i -band image, while the bottom inset shows those of the *HST* NICMOS NIC3 F160W image. North is up, and east is to the left.

respectively. For NGC 2681, we also used the *HST* NICMOS NIC3 F160W (H -band) image (Proposal ID 7919, PI: W. Sparks) inside $R \lesssim 3''$ to better correct for the galaxy's nuclear dust spiral and to avoid the saturated nucleus of the galaxy in the ACS F814W image.

2.1.2 SDSS

We obtained SDSS g -, i - and z -band images of NGC 2681, NGC 3945 and NGC 4371 from the SDSS Data Release 12 (DR12) database to better constrain the sky background and derive the radial color profiles for these three galaxies (see Figs. 1, 2 and 3, also Section 2.1.4).

2.1.3 Surface brightness profiles

Our data reduction steps, together with the surface brightness profile extraction procedures are described in detail in Dullo & Graham (2014, Sections 2.3 and references therein). We extracted major-axis surface brightness, ellipticity (ϵ), position angle (P.A.), and isophote shape parameter (B4) profiles from the *HST* and SDSS images using the IRAF ELLIPSE task (Jedrzejewski 1987). For each galaxy, ϵ and P.A. of the isophotes were set free to vary but we kept the centers fixed. We built composite profiles by combining high-resolution *HST* data typically inside $R \lesssim 70''$ with low-resolution ground-based SDSS data at larger radii. We

used high- and low-resolution profiles obtained using similar filters, i.e., we combine *HST* and SDSS light profiles by shifting the zero-point of the ACS/WFPC2 F814W data to match the SDSS i -band profiles, while the SDSS z -band data is zeropointed to the *HST* ACS F850LP profile (Fig. 4). These composite profiles typically extend to $R \sim 300''$. Our magnitudes are in the Vega magnitude systems.

2.1.4 Colors and mass-to-light (M/L) ratios

Here, we discuss the measurements of the colors and the stellar mass-to-light ratios listed in Table 4.

NGC 2681

We fit ELLIPSE to the SDSS- g , r -, and i -band images of NGC 2681, giving SDSS $g - i = 1.0$ color for the bulge. For a $g - i = 1$, the color calibration by Jordi et al. (2006) gives the Cousins $V - I = 1.04$. We also transformed the SDSS $g - r = 0.68$ and $r - i = 0.33$ colors from ellipse into $V - I$ (Jordi et al. 2006) and found that the $V - I = 1.04$ color is robust. Using $V - I = 1.04$ together with the color-age-metallicity- M/L diagram from Graham & Spitler (2009, their Figure A1), we found the V -band stellar mass-to-light ratio (M/L_V) = 2.25, which corresponds to $M/L_I = 1.58$ (Worthey 1994, his Table 5A).

NGC 3945

For NGC 3945, given the bulge and the pseudo-bulge have nearly the same color of $V - I = 1.27$ (Lauer et al. 2005, their Fig. 3) and together with the color-age-metallicity-

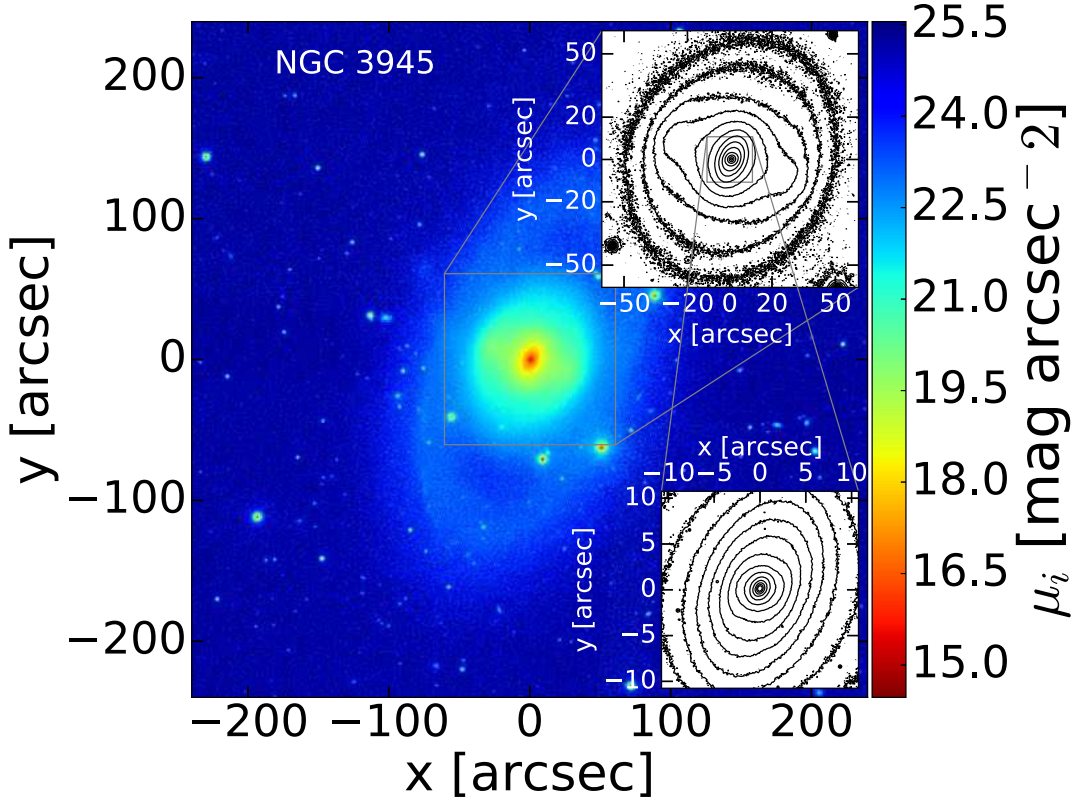


Figure 2. As Fig. 1, but showing the SDSS i -band and *HST* WFPC2 F814W images of NGC 3945.

M/L diagram (Graham & Spitler 2009) gives $M/L_V = 4.60$. This implies $M/L_I = 2.76$ for the bulge and pseudo-bulge (Worthey 1994, his Table 5A).

NGC 4371

As done for NGC 2681, we run ellipse on the SDSS- g , and i - band images of NGC 4371. This yielded $g - i = 1.1$ which corresponds to $V - I = 1.11$ (Jordi et al. 2006) and thus $M/L_V = 2.70$. Using Gallazzi & Bell (2009, their Fig. 10), $M/L_V = 2.70$ corresponds to $M/L_z = 1.13$. We note that the bulge and the pseudo-bulge have the same color for this galaxy.

2.2 Narrow-band observations

The only *HST* narrow-band images available in the HLA for our three galaxies is $H\alpha$ image of NGC 2681 (Proposal ID 9788, PI: L. Ho). Therefore, we observed NGC 3945 and NGC 4371 in the broad SDSS g -, r -bands and in the narrow-bands $H\beta$ $\lambda 4881$, $[O III]$ $\lambda 5032$, $H\alpha$ $\lambda 6589$, $[NII]$ $\lambda 6613$, and $[S II]$ $\lambda \lambda 6745, 6757$ using the auxiliary-port camera (ACAM) on the 4.2-m William Herschel Telescope (WHT) in La Palma. For NGC 2681, we obtained images using ACAM/WHT with the same filters as those used for NGC 3945 and NGC 4371 but excluding $H\alpha$. For each galaxy, we obtained three exposures per filter: 3×60 s in the broad bands and 3×300 s in the narrow bands. The galaxy images were taken during Director's Discretionary

Time (DDT, Proposal ID DDT2015-069) on the night of 2016 January 09 under good conditions. The seeing was typically $0''.8$. The imaging mode of ACAM has a plate scale of 0.25 arcsec/pixel and a circular, $8.3'$ diameter field of view (FOV).

2.2.1 Data reduction

HST images as retrieved from the HLA were processed using the standard HLA reduction pipeline. These images were bias-subtracted, sky-subtracted and flat-fielded. Our data reduction steps follow those described in Knapen et al. (2004) and Sánchez-Gallego et al. (2012, their Section 5), including bias subtraction, flat-fielding, sky background subtraction and the alignment of the science images. The images of each galaxy in each band are then combined. For each galaxy, all the narrow- and broad-band images were aligned using the IRAF tasks GEOMAP and GEOTRAN, with results to better than $0''.2$.

2.2.2 Continuum subtraction and flux calibration

In order to determine the emission lines fluxes, we followed similar continuum subtraction steps as outlined in Sánchez-Gallego et al. (2012, see references therein) and subtracted the underlying continuum component from the narrow-band images. In so doing, we first checked the difference between

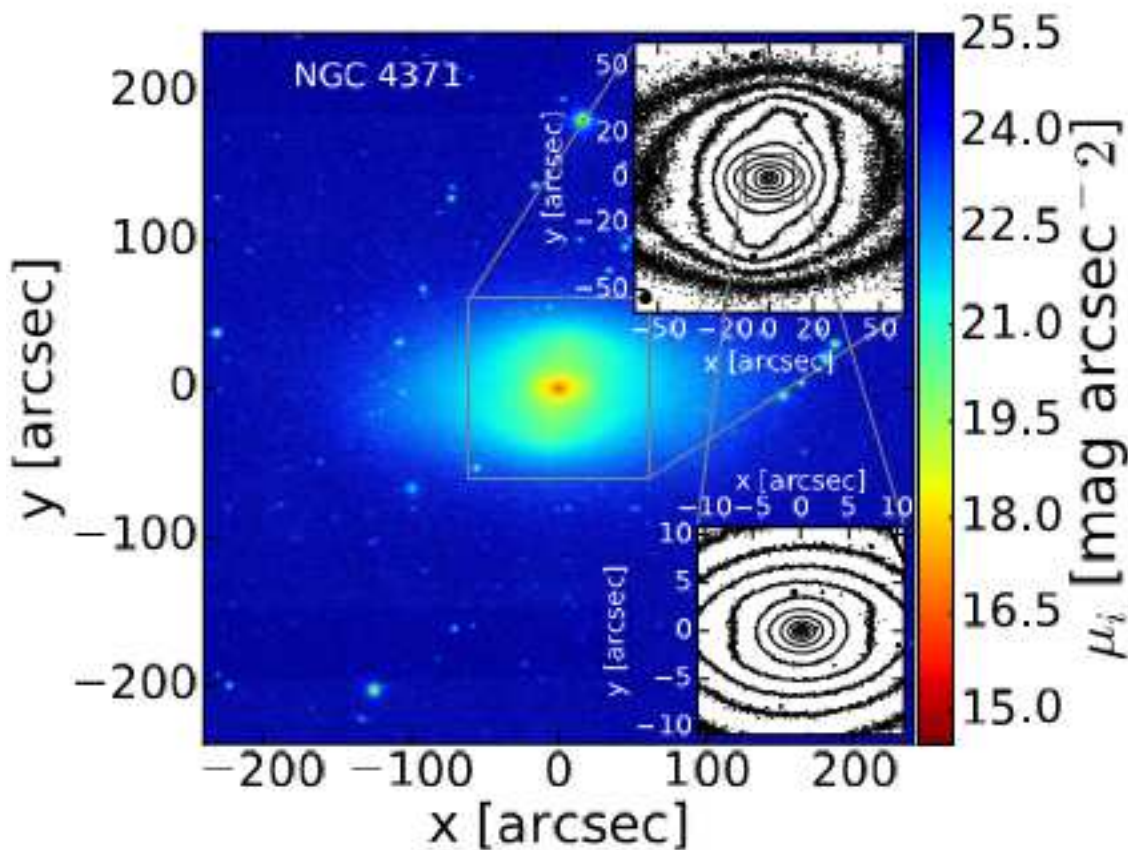


Figure 3. As Fig. 1, but showing the SDSS *i*-band and *HST* ACS F850LP images of NGC 4371.

the FWHMs of the point-spread functions (PSFs) of the narrow- and broad-band images. This difference was significant only for a handful of cases where we convolved the image with the good seeing with a Gaussian function to degrade it to the resolution of the poorest image. Next, we compared the intensities of the narrow- and broad-band images of each galaxy for the same pixels. That is, for each galaxy we compared the SDSS-*g* band pixel intensities with the corresponding narrow-band $H\beta$ $\lambda 4881$, $[O\ III]$ $\lambda 5032$ pixel intensities, and those in $H\alpha$ $\lambda 6589$, $[N\ II]$ $\lambda 6613$, and $[S\ II]$ $\lambda \lambda 6745, 6757$ with those in the SDSS-*r* band image. For NGC 2681, we compared the intensity of each pixel in the *HST* ACS F814W image with that of the same pixel in the *HST* ACS F658N image. Next, we perform linear regression fits to the narrow- and broad-band data points. The slopes of these linear fits correspond to the scale-factors between the narrow- and broad-band data. For a couple of images, we checked the validity of our scale-factor measurements by running ELLIPSE freely either on a broad- or narrow-band image and then using this solution to run ELLIPSE on the other image in the “no-fit” mode. Comparing the mean isophote intensities of the broad- and narrow-band galaxy images and fitting regression lines, we determined the scale-factors. While the results from these two objective methods agree well, we visually inspected each continuum subtracted image and iteratively corrected for continuum over-/under-subtraction by hand until an optimum continuum subtrac-

tion was achieved. Fig. 5 shows the continuum-subtracted images for each galaxy.

The emission line fluxes were calibrated using published nuclear spectral data in NED (Ho et al. 1995). These published spectra were extracted from $2'' \times 4''$ rectangular apertures in the nuclear regions of the galaxies. To determine the total emission line flux inside a $2'' \times 4''$ nuclear area in the continuum subtracted images, we run ELLIPSE after fixing the position angle to the P.A. of the slit provided in NED and setting $\epsilon = 0.5$. The total fluxes enclosed by an ellipse with semi-major axis $2''$ and a circle with radius $2''$ from ELLIPSE are used to calculate the flux inside the $2'' \times 4''$ area.

3 DECOMPOSING NGC 2681, NGC 3945 AND NGC 4371

Fig. 4 shows the major-axis surface brightness, ellipticity, P.A., and isophote shape parameter (B4) profiles of NGC 2681, NGC 3945 and NGC 4371. Fig. 4 also shows the 1D multi-component decomposition of the surface brightness profiles together with the fit residuals and the root-mean-square (rms) values for each galaxy. Because these modeled profiles cover a large range in radius ($R \sim 300''$), we minimise the systematic uncertainties. The best-fit parameters which describe the data are derived after iteratively minimizing the rms residuals using the Levenberg-Marquardt op-

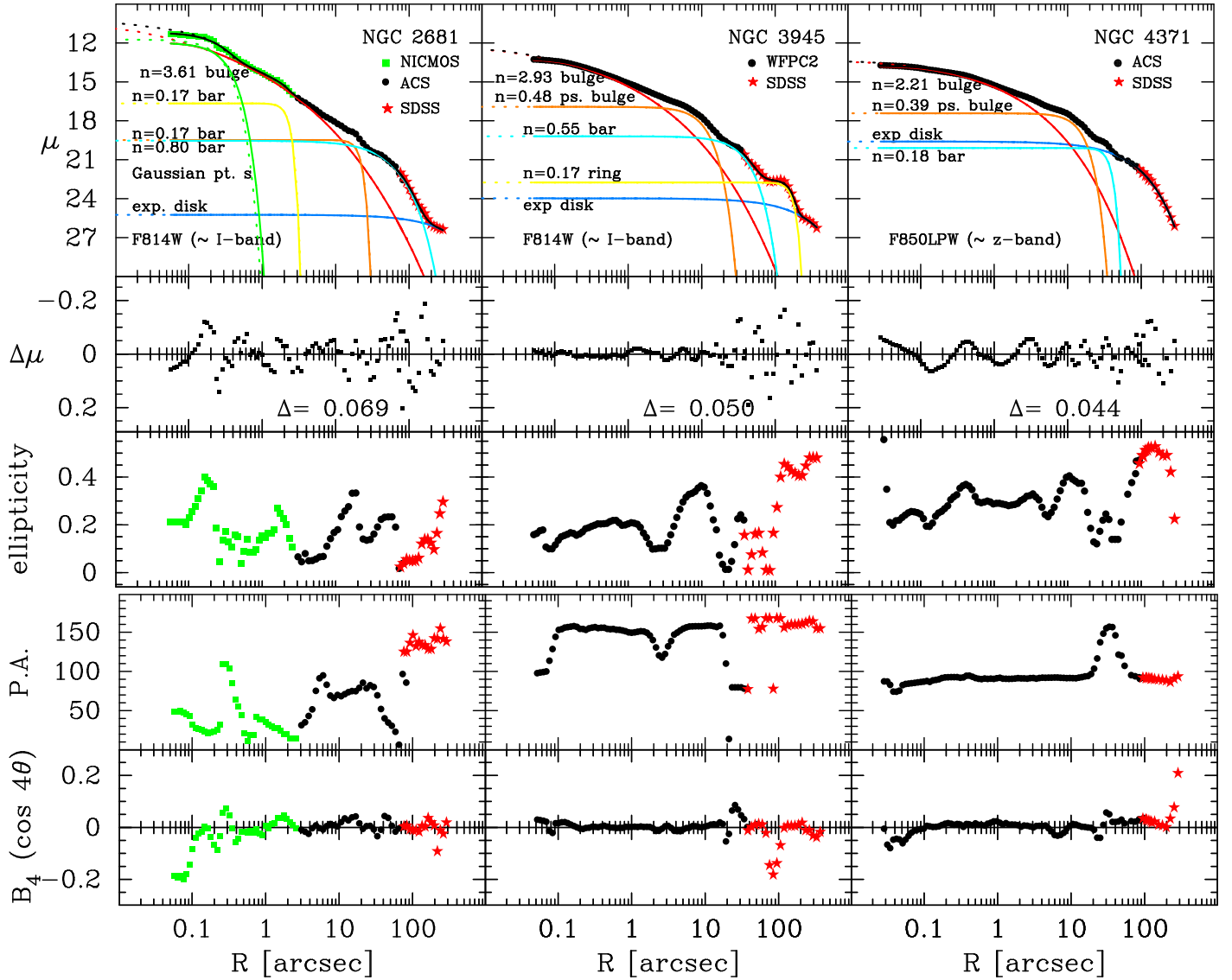


Figure 4. Multi-component decompositions of the composite (*HST* plus ground-based SDSS) surface brightness profiles of the S0 galaxies NGC 2681, NGC 3945 and NGC 4371 (from left to right). From top to bottom, the panels show multiple Sérsic model fits and the rms residuals about the fits, ellipticity (ϵ), position angle (P.A., measured in degrees from north to east) and isophote shape parameter (B_4) profiles for the galaxies. The models have been convolved with the PSF (see text for details). Solid and dashed curves show the PSF-convolved and -deconvolved profiles, respectively.

timisation algorithm (see Dullo & Graham 2014). For each iteration, the profiles of individual model components were convolved with the Gaussian PSF and then added to create the final model profile. The FWHMs of the PSFs were measured using several stars in the galaxy images. Table 2 lists the best-fit model parameters from the decompositions.

3.1 NGC 2681

The S0 galaxy NGC 2681 (Fig. 1) has complex structures which made the modelling of the light profile somewhat difficult. We fit a 6 component model (a Gaussian point source, three Sérsic bars plus a Sérsic bulge and an outer exponential disk) model to the *I*-band surface brightness profile. Detailed discussions of the Sérsic (1968) $R^{1/n}$ model are given by Graham & Driver (2005). Initial fits to the light profile

of NGC 2681 were performed after the parameters of the innermost Sérsic bar model were held fixed but the parameters of the remaining model components were left free. The outputs of a reasonable fit from these initial runs were used to re-run the code by allowing all the model parameters to be free. Fig. 4 shows the best fit with a small residual rms scatter of $0.069 \text{ mag arcsec}^{-2}$ (Table 2).

The isophotal profiles from the ELLIPSE fit (Fig. 4) and the *HST* F160W and SDSS *i*-band surface brightness contours (Fig. 1) confirm the profile decomposition. The ϵ and B_4 profiles have five local maxima (at radii $R \sim 0''.2 - 0''.3, 2'', 20'', 50''$ and $170''$) coincident with the point source, the three bars and the large-scale disk. The P.A. profile also shows significant twists ($\gtrsim 10^\circ$) coincident with the radii of the five local maxima of ϵ and B_4 .

The point source modelled with a PSF-convolved Gaus-

Table 2. Structural parameters

	NGC 2681 (<i>I</i>)	NGC 3945 (<i>I</i>)	NGC 4371 (<i>z</i>)
Bulge			
n	3.6	2.9	2.2
R_e	4.1	4.1	4.3
μ_e	16.90	17.67	17.56
Pseudo-bulge			
n_{Pb}	—	0.5	0.4
$R_{e,\text{Pb}}$	—	7.3	10.0
$\mu_{e,\text{Pb}}$	—	17.62	18.95
Bar_{Inner}			
n_{b1}	0.17	—	—
$R_{e,\text{b1}}$	1.5	—	—
$\mu_{e,\text{b1}}$	16.77	—	—
Bar_{Mid}			
n_{b2}	0.17	—	—
$R_{e,\text{b2}}$	13.8	—	—
$\mu_{e,\text{b2}}$	19.58	—	—
Bar_{Out}			
n_{b3}	0.8	0.6	0.2
$R_{e,\text{b3}}$	45.7	26.4	24.2
$\mu_{e,\text{b3}}$	20.94	20.06	20.22
Ring_{Out}			
n_{R}	—	0.17	—
$R_{e,\text{R}}$	—	112.6	—
$\mu_{e,\text{R}}$	—	22.87	—
Point source			
m_{pt}	14.17	—	—
Outer-disk			
μ_0	25.24	23.97	19.60
h	264.6	178.8	47.2

Notes.—Structural parameters obtained from our multiple Sérsic model fits to the major-axis surface brightness profiles of NGC 2681, NGC 3945 and NGC 4371. Note that for all model components, the half-light radius R_e is in arcsec and μ ($R = R_e$ and $R = 0$) is in mag arcsec⁻². Apparent magnitude of the point source m_{pt} is in mag.

sian function ($n = 0.5$) has an apparent F814W magnitude of 14.2 mag. Because of its high ellipticity ($\epsilon \sim 0.2-0.4$) and the residual structure at $R \sim 0''.1$ to $0''.3$, we also attempted modelling this inner component with an exponential disk model instead of a Gaussian function but the former resulted in an inferior fit. Actually, Balcells et al. (2007) warned that the NICMOS PSF has a secondary maximum at $R \sim 0''.23$ which may cause nuclear sources to appear extended.

The emission line diagnostic diagram in Fig. 6 (see Section 4) shows that NGC 2681 has LINER like emission from the nuclear region, $R \lesssim 2''.0$, due to an AGN but at larger radii the line emissions are from both star formation and an AGN (Section 4 and Fig. 5). Thus, it is not clear if the point source component is produced by an AGN, a compact nuclear star cluster or both, although intermediate-/low-luminosity ($M_B > -20.5$ mag) early-type galaxies tend to house nuclear star clusters rather than AGN (e.g., Côté et al. 2006; Dullo & Graham 2012; den Brok et al. 2014).

The $n = 3.6$ Sérsic bulge with $\epsilon \sim 0.1$ has a major-axis half-light effective radius of $R_e \sim 4''.1$ (Table 2). With a bulge-to-total flux ratio $B/T = 0.33$, it dominates the inner $R \sim 0''.3 - 10''$ regions. However, the inclusion of the inner $n = 0.17$ Sérsic bar component—with $R_e \sim 1''.5$ and a small $\text{Bar}_{\text{inn}}/T \sim 0.01$ —has improved the fit to the data (Tables 2 and 3). We note that the profiles of bars, lenses and

Table 3. Flux fractions

Galaxy	B/T	$\text{Bar}_{\text{inn}}/T$	$\text{Bar}_{\text{mid}}/T$	$\text{Bar}_{\text{out}}/T$	D_{out}/T	$\text{Pts.}/T$
(1)	(2)	(3)	(4)	(5)	(6)	(7)
NGC 2681	0.33	0.01	0.07	0.43	0.15	0.01
	B/T	B_{ps}/T	$\text{Bar}_{\text{out}}/T$	$\text{Ring}_{\text{out}}/T$	D_{out}/T	
NGC 3945	0.15	0.18	0.27	0.22	0.18	
	B/T	B_{ps}/T	Bar/T	D_{out}/T		
NGC 4371	0.18	0.29	0.22	0.32		

Notes.—Col. 1: galaxy name. Cols. 2-7: the total integrated fluxes were computed using the best-fit (major-axis) structural parameters (Table 2) and the ellipticity of each component (see Table 4 for (pseudo-)bulge ellipticities). We note that these flux ratios are not corrected for Galactic extinction, surface brightness dimming or internal dust attenuation.

rings are well described by the Sérsic model, typically with low $n \sim 0.2$, i.e., such profiles have very steep logarithmic slopes at larger radii compared to that of, for example, an exponential disk.

Our six-component decomposition is in good agreement with past works by Wozniak et al. (1995), Friedli et al. (1996), and Erwin & Sparke (1999, 2003). Wozniak et al. (1995) and Friedli et al. (1996) identified the two smaller bars via photometric analysis of ground-based images. Erwin & Sparke (1999) first detected all three bars of NGC 2681 from ellipse fits and unsharp masking to *HST* and ground-based images.

The analysis of a ground-based K_s image of NGC 2681 by Laurikainen et al. (2005) revealed a lens, and a triple bar structure that are additional to the underlying host galaxy bulge+disk light. Excluding the innermost bar, they performed a 5-component (2D) decomposition into a bulge, a disk, two bars and a lens. The lens component (at $R \sim 5''$) detected by Laurikainen et al. (2005) from their K_s -band image is not obvious from our *I*-band data. The Laurikainen et al. (2005) ground-based image with a seeing of $1.1''$ covering $R \sim 100''$ did not have sufficient resolution to resolve the point source that we modelled. They modelled the bulge component of NGC 2681 using a Sérsic model with $n = 2.2$ and $R_e = 1''.8$. This is in contrast to the $n = 3.6$, $R_e \sim 4''.1$ Sérsic bulge from this work. Finally, Richings et al. (2011) fit a single component Sérsic bulge model to the $R \lesssim 10''$ (point source, bar plus bulge) light profile of NGC 2681 (see Fig. 4), yielding an incorrect $n = 12.4$ for the bulge.

3.2 NGC 3945

This S0 galaxy has two concentric bars (Wozniak et al. 1995; Erwin & Sparke 1999) and a pseudo-bulge (Kormendy 1979, 1982). The inner bar in the region $R \sim 2'' - 3''$ which is exhibited as local minima in the ϵ , P.A. and B_4 profiles is weak along the major-axis (Figs. 2, 4, and 5). The galaxy also has a lens at the radius of the large bar (Fig. 5). Excluding the inner bar component and the lens, we performed a 5-component decomposition into a bulge, a disk, a 'pseudo-bulge', a bar, an outer ring and a large-scale disk using a

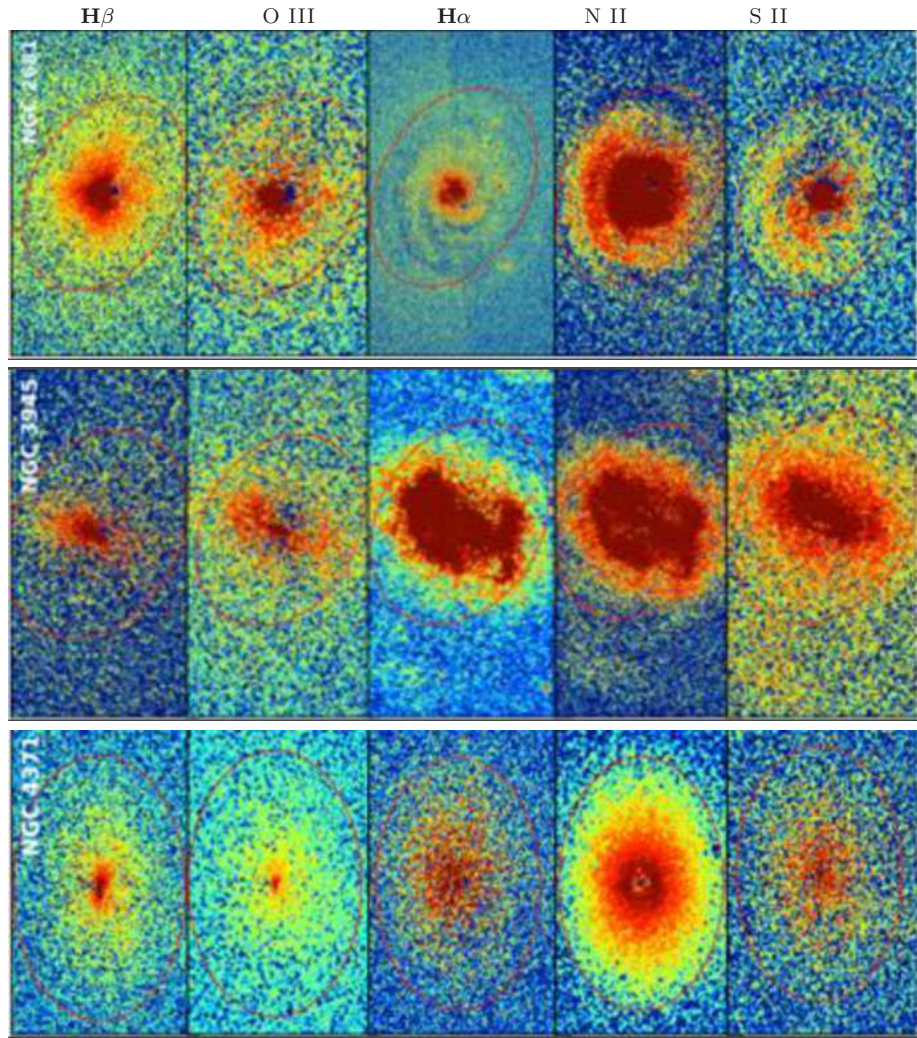


Fig. 5.— $H\beta$ $\lambda 4881$, $[O\ III]$ $\lambda 5032$, $H\alpha$ $\lambda 6589$, $[N\ II]$ $\lambda 6613$, and $[S\ II]$ $\lambda\lambda 6745, 6757$ continuum-subtracted images of NGC 2681 (first row), NGC 3945 (second row) and NGC 4371 (third row). The nature of the nuclear activities of these galaxies are shown in the BPT diagram (Fig. 4) by measuring the emission line ratios computed within 9 different elliptical apertures. The red ellipse indicates the largest aperture with semi-major axis $R \sim 20''$ and the pertaining galaxy position angle (See Section 4).

Table 4. Galaxy properties

Galaxy	$V - I$	M/L	$\epsilon/\log M_*$ (bulge)	$\epsilon/\log M_*$ (pseudo-bulge)
(1)	(2)	(3)	(4)	(5)
NGC 2681	1.04	1.58 (<i>I</i>)	0.12/10.04	—
NGC 3945	1.28	2.76 (<i>I</i>)	0.22/10.00	0.35/10.10
NGC 4371	1.11	1.13 (<i>z</i>)	0.30/9.44	0.42/9.64

Notes.— Col. 1: galaxy name. Measurements of the (pseudo-)bulge $V - I$ color (Col. 2) and the stellar mass-to-light M/L ratio (Col. 3) are discussed in Section 2.1.4. We calculated the total luminosities of the bulge and the pseudo-bulge using the best fitting Sérsic model parameters (Table 2) and the pertaining ellipticities ϵ (Cols. 4 and 5). After correcting these luminosities for galactic extinction and surface brightness dimming, we calculated the stellar masses of the bulge (Col. 4) and the pseudo-bulge (Col. 5) using the M/L ratios (Col. 3).

four Sérsic+exponential disk model. This yielded a good fit as revealed by the small rms residual scatter of $0.050\text{ mag arcsec}^{-2}$ (Fig. 4, Table 2). The Sérsic fit to the bulge in Fig. 4 gives $n \sim 2.8$ and $R_e \sim 3.6''$. The disk ‘pseudo-bulge’ component with $\epsilon \sim 0.22 \pm 0.16$ which dominates the profile at $R \sim 3'' - 12''$ follows a Gaussian ($n = 0.5$) light distribution with $R_e \sim 7''.3$. We refer to the intermediate-scale disk components of NGC 3945 and NGC 4371 as ‘pseudo-bulges’ adopting the Erwin et al. (2015) classification (see also Section 3.3).

The five-component decomposition can be compared to those in the literature (Erwin et al. 2003b, 2015; Lauer et al. 2005; Richings et al. 2011; Laurikainen et al. 2010). For instance, Erwin et al. (2015, their Fig. 4, see also their Fig. 3) excluded the bars and fit a Sérsic+ two-exponential model to the $\sim 20'' - 30''$ major-axis cut *HST* light profile without accounting for the PSF, concluding that a pseudo-bulge and a classical bulge coexist in NGC 3945. While we agree with this conclusion, our fit differs from theirs. For example, the luminosity of the $n = 2.02$ Sérsic bulge with $R_e = 1.24$

Richings et al. (2011) fit a double-Sérsic model (i.e., an inner $n \sim 1.57$, $R_e \sim 1.1$ Sérsic model plus and outer $n \sim 1.04$, $R_e \sim 9.3$ Sérsic model) to the *HST* WFPC2 F814W brightness profile of NGC 3945. Clearly, the treatment of a five-component system as a two-component system by Richings et al. (2011) is inadequate, and indeed their fit disagrees with our decomposition.

3.3 NGC 4371

This S0 galaxy has a single bar (Figs. 3, 4, see also Erwin et al. 1999). Fig. 4 shows a Sérsic bulge + Sérsic pseudo bulge + Sérsic bar + exponential disk model fit to the ACS z -band light profile with a small rms residual scatter of $0.044 \text{ mag arcsec}^{-2}$. This four component decomposition is somewhat similar to that of NGC 3945 but the latter has a fifth model component that accounts for the galaxy’s outer ring. For NGC 4371, we did not include the ring component at $R \sim 10''$ which is dominated by the pseudo-bulge light. As such, the pseudo-bulge component model may wrongly contain additional flux from this ring.

There appears to be some evidence for excess light from $R \sim 0.35''$ to $0.5''$, visible in the residual structure from the fit (Fig. 4). In this region, the ellipticity also rises to a local maximum of 0.37. This apparent excess light is due to the nuclear dust ring which reduces the surface brightness at $R \sim 0.45''$ - $0.7''$, as seen in the archival *HST* ACS $F475W$ image, although it is not obvious from the eyeball inspection of the *HST* ACS $F814W$ image that we analysed in this work (see Comerón et al. 2010).

This galaxy’s bulge and pseudo-bulge are modelled using Sérsic models with $n = 2.21$ and $n = 0.39$, respectively. For comparison, Erwin et al. (2015, their Fig. 6) remarked the coexistence of a bulge and a pseudo-bulge inside NGC 4371. They measured $n = 2.18$ for their Sérsic bulge component and fit a broken exponential model for the pseudo-bulge. Laurikainen et al. (2010) fit a Sérsic model with $n = 2.60$ to the bulge profile and the Ferrer function to the pseudo-bulge profile which they refer to as an inner disk. In contrast, Gadotti et al. (2015, their Figs. 4,5) combining kinematic, stellar population and structural analyses of NGC 4371 argued that the galaxy has a diskly nuclear component, instead of a bulge. They fitted exponential functions to this nuclear component and the galaxy’s inner disk. However, Fig. 4 shows a bulge with $R_e \sim 361 \text{ pc}$ that dominates at $R \lesssim 5''$, in excellent agreement with the Gadotti et al. stellar population maps which reveal a high concentration of old stars over the $R \lesssim 5''$ region (Section 5.1).

4 THE BPT DIAGRAMS

Building on the careful structural decompositions (Section 3), in this section we explore the emission line processes and gas ionisation mechanisms in the nuclear regions of NGC 2681, NGC 3945 and NGC 4371 (Fig. 5).

First constructed by Baldwin, Phillips & Terlevich (1981), the $[\text{O III}]/\text{H}\beta$ versus (i) $[\text{N II}]/\text{H}\alpha$, (ii) $[\text{S II}]/\text{H}\alpha$ and (iii) $[\text{O I}]/\text{H}\alpha$ plots which are now commonly referred to as the BPT diagrams were designed to distinguish gas ionisation in galaxies by hot OB stars, AGN and interstellar shocks. These diagrams have now become standard diag-

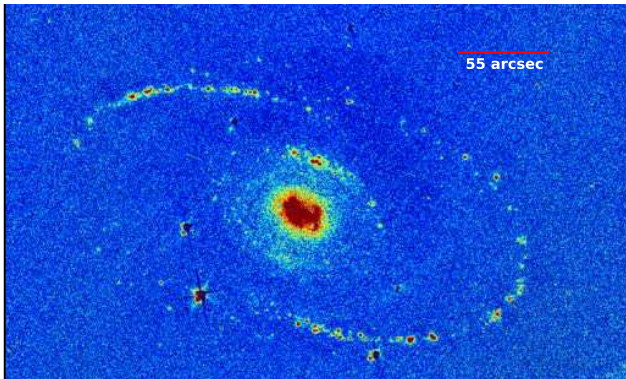


Figure 5. *Continued.* $\text{H}\alpha$ continuum-subtracted image of NGC 3945 showing the large-scale ring and the lens at the radius of the large bar.

(Erwin et al. 2015) is factor three fainter than ours (see Section 5.1 for further details). Furthermore, we find that the pseudo-bulge has a Gaussian ($n=0.5$) stellar light distribution rather than an exponential one. This discrepancy could arise in part from the treatment of the PSF and the difference between the global ellipse fit profile used in this work and the major-axis cut profile used by Erwin et al. (2015).

Laurikainen et al. (2010) fit a 2D, six-component (bulge + inner lens+inner bar + outer bar + outer lens + outer disk) model to the $R \sim 120''$ K_s -band image. While their $n \sim 2.9$ Sérsic fit for the bulge agrees with ours, they did not identify the highly elliptical (pseudo-bulge) component from $R \sim 3'' - 12''$.

Having excluded additional nuclear components, Lauer et al. (2005, their Fig. 3; also Krajnović et al. 2013) fit the Nuker model to inner $10''$ *HST* profile. This fit poorly matches the data and it shows a clear residual structure.

nostic tools for discriminating between star forming galaxies and AGN (e.g., Kewley et al. 2001, 2006, 2013; Kauffmann et al. 2003).

Having measured the fluxes of the Balmer lines $H\beta$ $\lambda 4881$, $H\alpha$ $\lambda 6589$, and the forbidden lines $[O III] \lambda 5032$, $[N II] \lambda 6613$, and $[S II] \lambda \lambda 6745, 6757$ for NGC 2681, NGC 3945 and NGC 4371, in Fig. 6 we show the positions of each galaxy in the $[O III]/H\beta$ versus $[N II]/H\alpha$ and $[O III]/H\beta$ versus $[S II]/H\alpha$ diagnostic diagrams. For each galaxy, we measured the total fluxes within 9 different elliptical apertures of semi-major axes $R = 1'', 2''.25, 3'', 4'', 5'', 8'', 10'', 15'',$ and $20''$ centred at the nucleus to investigate the dominant ionisation mechanisms in the nuclear and circumnuclear regions. In order to show this, in Fig. 6 the sizes of the data points (symbols) increase when the aperture size increases.

In Fig. 6a, the ‘pure star-forming galaxies’ occupy the region below the Kauffmann et al. (2003) demarcation line, while ‘composite’ galaxies occupy the region outside the Kauffmann et al. line and below the Kewley et al. (2001) line. The narrow line emission of composite galaxies is due to contribution from both AGN activity and star formation. The ‘pure AGN zone’ above the Kewley et al. (2001) encompasses low ionization nuclear emission regions (LINERs, Heckman 1980) and Seyfert galaxies.

Fig. 6a shows that NGC 2681, NGC 3945 and NGC 4371 fall outside the ‘pure star-forming galaxy’ zone in the BPT diagram. The trend in Fig. 6a is that NGC 2681 has LINER type emission within $R \sim 3''$ (see Wozniak et al. 1995, Ho et al. 1995; Böker et al. 1999; Cappellari et al. 2001) but the fractional contribution to the emission line from star formation increases with increasing aperture, in agreement with the presence of the point source and nuclear bar in this galaxy (see Section 3.1 and Fig. 4). This in contrast to NGC 3945 and NGC 4371, which show an opposite trend where the contributions of the emission lines are dominated by the AGN for $R \gtrsim 2''$. We note that NGC 4371 has the weakest emission lines of the three galaxies.

Akin to Fig. 6a, Fig. 6b shows that the emission of NGC 3945 and NGC 4371 are LINER-like. On the other hand, NGC 2681 is dominated by LINER-like activity within $R \lesssim 2''$ but outside this region (i.e., from $R \sim 2''$ to $20''$) the contribution from stellar photoionisation becomes significant.

5 DISCUSSION

5.1 Bulge/pseudo-bulge in NGC 2681, NGC 3945 and NGC 4371

The fits in Section 3 reveal that NGC 2681, NGC 3945 and NGC 4371 contain bulges that have Sérsic indices $n \sim 2.2$ to 3.6 . In addition, NGC 3945 and NGC 4371 have intermediate-scale disk ($\epsilon \gtrsim 0.3$) pseudo-bulges that we modelled using the Sérsic model with low Sérsic indices $n \sim 0.48$ and 0.39 , respectively, rather than an exponential ($n = 1$) disk profile as done by Laurikainen et al. (2010), Erwin et al. (2015) and Gadotti et al. (2015). Forcing an exponential ($n = 1$) disk profile overestimates the actual luminosities of these low n ($\lesssim 0.5$) pseudo-bulges which dominate the intermediate regions of the galaxies rather than at large radii like large-scale disks do. On the other hand,

the bulge light in NGC 3945 and NGC 4371 dominates over the pseudo-bulge light at both small and large radii (Fig 4). As such these bulges do not reside within the pseudo-bulges (although see Erwin et al. 2015).

All of our bulges (and pseudo-bulges) have Sérsic indices $\gtrsim 2$ (and < 2), in agreement with the ‘pseudo-bulge’ ($n \lesssim 2$) versus ‘classical bulges’ ($n \gtrsim 2$) dichotomy (e.g., Fisher & Drory 2008). However, the robustness of such a Sérsic index-based division among bulges is highly disputed (e.g., Athanassoula 2005; Graham 2013, 2014).

The dichotomy in the properties between pseudo-bulges and classical bulges is attributed to their formation mechanisms. Pseudo-bulges are thought to have formed via inward funnelling of disk materials catalysed by non-axisymmetric features, for example bars and rings (e.g., Pfenniger & Friedli 1991; Kormendy & Kennicutt 2004) while classical bulges (hereafter referred to as bulges), akin to elliptical galaxies, are believed to be products of violent hierarchical merging processes (e.g., Toomre & Toomre 1972; Kauffmann et al. 1996) or/and a rapid dissipative collapse (Eggen et al. 1962). Also, those massive present-day bulges, typically with $M_* \gtrsim 10^{11} M_\odot$ and $R_e \lesssim 2$ kpc, might be descendants of the compact, massive high-redshift ($z \sim 2$) early-type galaxies² (Graham 2013, Dullo & Graham 2013; Graham, Dullo & Savorgnan 2015; de la Rosa et al. 2016).

Table 3 lists the fractional luminosities of the (pseudo-)bulges plus other model components in NGC 2681, NGC 3945 and NGC 4371. For each component, the total integrated flux was computed using the best-fit (major-axis) structural parameters (Table 2) and the corresponding ellipticity. These new flux measurements improve upon past works which used ground-based data or/and fitted a 2-component bulge plus disk model because our measurements are based on careful multi-component decompositions of high-resolution *HST* plus ground-based SDSS data, and accounting for (i) the bulge, pseudo-bulge, disk, bar, lens, and point-source of the galaxies and (ii) the PSF convolution.

I-band bulge-to-total flux (B/T) ratio of NGC 2681 is 0.33, considerably higher than those of NGC 3945 (*I*-band $B/T \sim 0.15$) and NGC 4371 (*z*-band $B/T \sim 0.18$), and broadly consistent with Laurikainen et al. (2010; K_s -band $B/T = 0.24$). For NGC 2681, the large-scale bar contains a significant fraction of the galaxy light ($Bar_{out}/T \sim 0.43$), compared to the bulge ($B/T \sim 0.33$) and the disk ($D/T \sim 0.18$). The two smaller bars and the point source are relatively less luminous, adding up to 10% of the total galaxy flux.

For NGC 3945 and NGC 4371, the bulges are fainter than all the other components of the galaxies (Fig. 4, Tables 2, 3). Our B/T ratios for these two galaxies ($(B/T)_{N3945} \sim 0.15$, $(B/T)_{N4371} \sim 0.18$) are up to a factor of 3 higher than those reported by Erwin et al. (2015, $(B/T)_{N3945} \sim 0.06$, $(B/T)_{N3945} \sim 0.09$), their Table 5). On the other hand, the B/T ratio for NGC 4371 is in good agreement with Laurikainen et al. (2010, $B/T = 0.20$), but

² Daddi et al. (2005) found compact $R_e \lesssim 2$ kpc, massive ($M_* \gtrsim 10^{11}$) early-type galaxies at $z \gtrsim 1.4$, noting the sizes of these objects are much smaller than local elliptical galaxies of comparable mass.

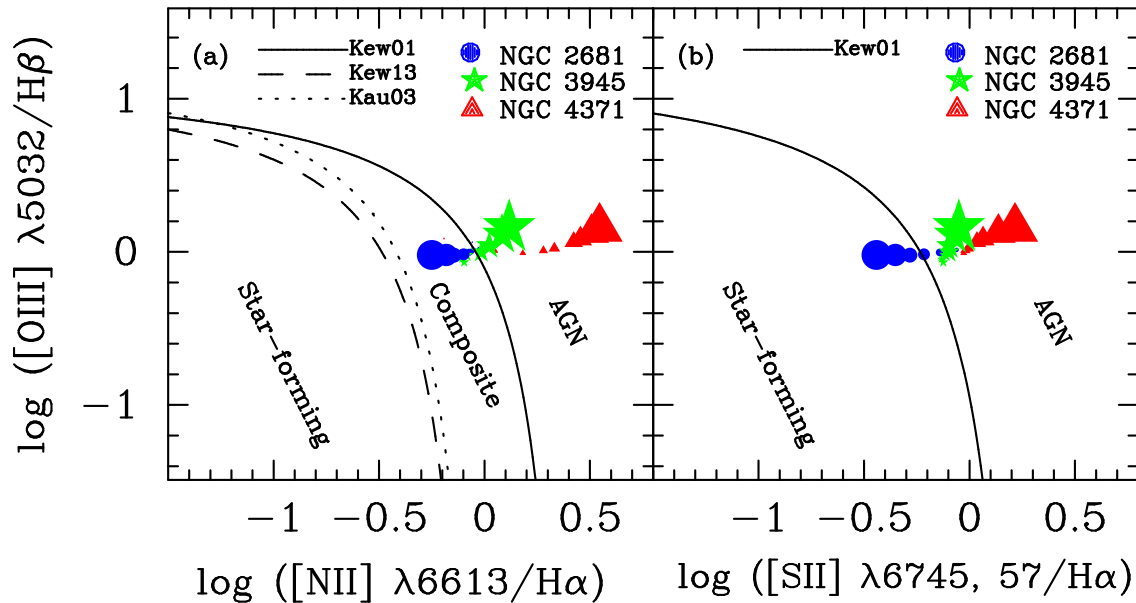


Figure 6. Emission line ratio diagnostic diagrams separating AGN and star forming galaxies. (a) The $[\text{O III}]/\text{H}\beta$ versus $[\text{N II}]/\text{H}\alpha$ diagram. The solid curve traces the Kewley et al. (2001) theoretical extreme starburst boundary, while the dotted and dashed curves denote the empirical dividing lines adopted by Kauffmann et al. (2003) and Kewley et al. (2013), respectively. (b) The $[\text{O III}]/\text{H}\beta$ versus $[\text{S II}]/\text{H}\alpha$ diagram. The solid curve shows the boundary from Kewley et al. (2001). In each panel, the sizes of the symbols increase when the aperture size used for measuring the flux increases (see the text for details).

because the 2D decomposition by Laurikainen et al. did not identify the pseudo-bulge in NGC 3945 their $B/T = 0.35$ ratio for that galaxy is higher than ours. It is worth noting that the bars, rings and the point source pertaining to our three galaxies add up to more than 20% of the total galaxy luminosities, underscoring the importance of including these components in the decomposition of multicomponent galaxies.

Before estimating the stellar masses of the bulges and pseudo-bulges in Table 4, we corrected their luminosities for galactic extinction and surface brightness dimming. The bulges of NGC 2681, NGC 3945 and NGC 4371 are compact (i.e., half-light radii $R_e \sim 229.6$ pc to 385.4 pc) and have stellar masses in the range $M_* \sim 0.28 \times 10^{10} - 1.1 \times 10^{10} M_\odot$. Assuming a lower stellar mass limit of $1 \times 10^{10} M_\odot$ for compact, massive high- z galaxies (e.g., Barro et al. 2013), implies that the bulges of NGC 2681 and NGC 3945 (see Table 4) might be local counterparts to compact high- z galaxies (Dullo & Graham 2013, their Fig. 5; Graham, Dullo & Savorgnan 2015, their Fig. 3). The bulge of NGC 4371 is less massive than the aforementioned mass limit. Furthermore, the (pseudo-)bulge-total flux ratios, masses and Sérsic indices n of the bulges and pseudo-bulges of our three barred S0 galaxies are similar to those of other spiral and lenticular galaxies (see e.g., Balcells et al. 2007; Graham & Worley 2008; Laurikainen et al. 2010, their Figs. 4, 5, and 6; Kormendy et al. 2012, their Table 1; Graham 2014, his Fig. 5; Erwin et al. 2015, their Figs. 8, 10). This similarity is unsurprising because the (pseudo-)bulge-to-total flux ratio for S0s can have any value between 1 and 0 (e.g., Laurikainen et al. 2010) and it does not imply that multiple evolutionary paths are not possible for S0s (e.g., Laurikainen et al. 2010; Dullo & Graham 2013; Graham, Dullo & Savorgnan 2015; Erwin et al. 2015).

5.2 Formation of NGC 2681, NGC 3945 and NGC 4371

Given that the sizes (as measured by the half-light radii R_e) of all the structural components of our galaxies, except the outer disks and the large-scale ring of NGC 3945, are smaller than those of the large-scale bars, one can simply envisage that these galaxies are created via bar-related processes. Small-scale bars and rings facilitate the gas supply to nuclear regions of the galaxies (e.g., Shlosman et al. 1989). In favor of this argument are (i) the presence of pseudo-bulges in NGC 3945 and NGC 4371 and (ii) the LINER nuclear emission of the double- and triple-barred galaxies (NGC 3945 and NGC 2681), compared to the weak nuclear emission of the single-bar galaxy NGC 4371 (Section 4). For NGC 2681, the point source and the winding nuclear stellar spiral seen in continuum subtracted images (Figs. 5, 6) are also consistent with a bar-driven formation scenario.

However, bar-related mechanisms cannot account for the bulges of NGC 2681, NGC 3945 and NGC 4371. For example, the bulge of NGC 2681 has a high central light concentration, as indicated by $n = 3.6$, suggestive of a classical ($R^{1/4}$) bulge. Similarly, the bulge of NGC 3945 with $n = 2.9$ and a low ellipticity ($\epsilon \sim 0.22$) favors a merger-built scenario. Also, the stellar kinematics by Erwin et al. (2015, their Fig. 4d) for NGC 3945 shows that the ratio of rotation velocity to velocity dispersion is low (i.e., $V/\sigma \lesssim 1$) in the inner regions where the bulge dominates (i.e., $R \lesssim 3''$), supporting a merger origin for the galaxy's bulge. As noted above in Section 5.1, the bulges of NGC 2681 and NGC 3945 occupy the same area as the $z \sim 2 \pm 0.5$ compact spheroids in the size-mass diagram, although, all our bulges contain masses that are smaller than the conservative lower stellar mass limits adopted for high- z compact galaxies ($0.7 \times 10^{11} M_\odot$), for example, by Graham et al. (2015, and references therein).

Therefore, our three galaxies may rather have had their bulges built at high redshift through violent major mergers, and the formation of the large-scale disks, pseudo-bulges, bars and rings subsequently ensues. In excellent agreement with this picture, the MUSE stellar population maps by Gadotti et al. (2015, their Figs. 13, 14) for NGC 4371 clearly show that the regions where the bulge dominates over the pseudo-bulge (i.e., the inner $5''$ plus the region immediately outside the pseudo-bulge, see Fig. 4) have the highest concentration of old (>8 Gyr) stars in the galaxy, as remarked upon by Gadotti et al. (2015).

Overall, our results suggest that the barred S0 galaxies NGC 2681, NGC 3945 and NGC 4371 likely have a complex formation and evolutionary history. The pseudo-bulges have formed slowly out of the disk materials through the actions of bars and rings which drive gas inflow for fuelling the AGN while the spheroidal components (i.e., bulges) are consequences of violent mergers or a rapid gravitational collapse that happened earlier. Further investigation of whether all the bulges that we have identified are actually dominated by stars that are older than those of the pseudo-bulges, bars, rings and outer disks, as is the case for NGC 4371 (Gadotti et al. 2015) together with the analysis of the age differences between the pseudo-bulges and the bars/outer disks are desirable.

6 CONCLUSIONS

We have extracted composite major-axis surface brightness profiles and isophotal parameters for three barred S0 galaxies (NGC 2681, NGC 3945 and NGC 4371) that have complex central structures using high-resolution *HST* WFPC2, ACS and NICMOS plus ground-based SDSS images. Consistent with earlier published isophotal analysis, we found that NGC 2681 hosts three bars, while NGC 3945 and NGC 4371 are double- and single-barred galaxies, respectively. We performed detailed, four- to six-component (pseudo-)bulge/disk/bar/ring/point source decompositions of the composite profiles covering a large radial range of $\sim 300''$, quantifying robustly the global and central structural properties of the galaxies. We fit an exponential function to the outer disk plus a Gaussian function to the point source, and each of the other components is modelled with a Sérsic model. To our knowledge, this is the first time that such global decompositions have been made for these three galaxies. In addition, measuring the $H\beta$ $\lambda 4881$, $[O\ III]$ $\lambda 5032$, $H\alpha$ $\lambda 6589$, $[N\ II]$ $\lambda 6613$, and $[S\ II]$ $\lambda\lambda 6745, 6757$ line fluxes enclosed inside 9 different elliptical apertures of semi-major axes ($R = 1'', 2''.25, 3'', 4'', 5'', 8'', 10'', 15'',$ and $20''$), we constructed the standard BPT diagnostic diagrams to distinguish between line emission produced by star formation, an AGN or composite AGN plus star formation processes. Our principal findings are as follows.

(1) The decompositions yield good fits to the galaxy data. The average rms residual scatter is ~ 0.05 mag arcsec 2 . We provide robust structural parameters for all the galaxy components. For our galaxies, we found that all the components except the outer bar, ring and disk have effective half-light radii $R_e \lesssim 1$ kpc.

(2) An intermediate-scale disk ($\epsilon \gtrsim 0.3$) component (which we refer to as ‘pseudo-bulge’) and a bulge coexist

within NGC 3945 and NGC 4371, confirming the conclusion of Erwin et al. (2015). However, in contrast to past works we found that these pseudo-bulges follow a low n ($\lesssim 0.5$) Sérsic model profile instead of an exponential ($n = 1$) profile. Fitting an exponential profile to what is actually a Sérsic profile with a low n overestimates the luminosity and mass of the pseudo-bulge. The bulges of our three galaxies have Sérsic indices of $2.2 - 3.6$.

(3) We have presented new fractional luminosities for the (pseudo-)bulges and other model components of NGC 2681, NGC 3945 and NGC 4371. We found that the bulges of our galaxies are compact (i.e., half-light radii $R_e \sim 229.6$ pc to 385.4 pc) and have stellar masses of $M_* \sim 0.28 \times 10^{10} - 1.1 \times 10^{10} M_\odot$.

(4) The nuclear regions of NGC 2681, NGC 3945 and NGC 4371 lie well outside the pure star-forming galaxy zone in the BPT diagram. Instead, NGC 2681 has LINER-type emission inside $R \sim 3''$ but the emission lines due to star formation become increasingly significant when the aperture size is increased, consistent with the presence of the point source and nuclear bar in this galaxy. This trend is reversed for NGC 3945 and NGC 4371 where the contributions of the emission lines are dominated by the AGN over $R \gtrsim 2''$. NGC 4371 has the weakest emission lines of the three galaxies.

(5) Our results suggest that the bulges of the three galaxies have formed via an earlier violent merging while the disks form over time through gas accretion and bar-driven perturbations could create pseudo-bulges, bars, rings and point sources. Nested bars are common, with around one third of all barred galaxies containing at least one additional smaller bar, and in future work we will analyse more of such systems in order to categorise them in more detail, and compare them in detail with dynamical models.

7 ACKNOWLEDGMENTS

BTD & JHK acknowledge financial support from the Spanish Ministry of Economy and Competitiveness (MINECO) under grant number AYA2013-41243-P. JHK thanks the Astrophysics Research Institute of Liverpool John Moores University for their hospitality, and the Spanish Ministry of Education, Culture and Sports for financial support of his visit there, through grant number PR2015-00512. We are grateful for F. Tabatabaei for her support with the observations. Based on observations made with the WHT under Director’s Discretionary Time of Spain’s Instituto de Astrofísica de Canarias. The WHT is operated on the island of La Palma by the Isaac Newton Group in the Spanish Observatorio del Roque de los Muchachos of the Instituto de Astrofísica de Canarias. Based on observations made with the NASA/ESA Hubble Space Telescope, and obtained from the Hubble Legacy Archive, which is a collaboration between the Space Telescope Science Institute (STScI/NASA), the Space Telescope European Coordinating Facility (ST-ECF/ESA) and the Canadian Astronomy Data Centre (CADCA/NRC/CSA). This research has made use of the NASA/IPAC Extragalactic Database (NED) which is operated by the Jet Propulsion Laboratory, California Institute of Technology, under contract with the National Aeronautics and Space Administration. Funding for the Sloan Digital Sky Survey IV has been

provided by the Alfred P. Sloan Foundation, the U.S. Department of Energy Office of Science, and the Participating Institutions. SDSS-IV acknowledges support and resources from the Center for High-Performance Computing at the University of Utah. The SDSS web site is www.sdss.org.

SDSS-IV is managed by the Astrophysical Research Consortium for the Participating Institutions of the SDSS Collaboration including the Brazilian Participation Group, the Carnegie Institution for Science, Carnegie Mellon University, the Chilean Participation Group, the French Participation Group, Harvard-Smithsonian Center for Astrophysics, Instituto de Astrofísica de Canarias, The Johns Hopkins University, Kavli Institute for the Physics and Mathematics of the Universe (IPMU) / University of Tokyo, Lawrence Berkeley National Laboratory, Leibniz Institut für Astrophysik Potsdam (AIP), Max-Planck-Institut für Astronomie (MPIA Heidelberg), Max-Planck-Institut für Astrophysik (MPA Garching), Max-Planck-Institut für Extraterrestrische Physik (MPE), National Astronomical Observatory of China, New Mexico State University, New York University, University of Notre Dame, Observatório Nacional / MCTI, The Ohio State University, Pennsylvania State University, Shanghai Astronomical Observatory, United Kingdom Participation Group, Universidad Nacional Autónoma de México, University of Arizona, University of Colorado Boulder, University of Oxford, University of Portsmouth, University of Utah, University of Virginia, University of Washington, University of Wisconsin, Vanderbilt University, and Yale University.

REFERENCES

- Ann, H. B., & Thakur, P. 2005, *ApJ*, 620, 197
- Athanassoula, E. 1992, *MNRAS*, 259, 345
- Athanassoula, E. 2005, *MNRAS*, 358, 1477
- Balcells M., Graham A. W., Peletier R. F., 2007, *ApJ*, 665, 1084
- Baldwin, J., Phillips, M., & Terlevich, R. 1981, *PASP*, 93, 5
- Blakeslee, J. P., Lucey, J. R., Tonry, J. L., et al. 2002, *MNRAS*, 330, 443
- Barro, G., Faber, S. M., Pérez-González, P. G., et al. 2013, *ApJ*, 765, 104
- Böker, T., Calzetti, D., Sparks, W., et al. 1999, *ApJS*, 124, 95
- Buta, R., & Crocker, D. A. 1993, *AJ*, 105, 1344
- Buta, R., Sheth, K., Athanassoula, E., et al. 2015, *ApJS*, 217, 32
- Cappellari, M., Bertola, F., Burstein, D., Buson, L. M., Greggio, L., & Renzini, A. 2001, *ApJ*, 551, 197
- Cisternas M., Sheth K., Salvato M., Knapen J. H., Civano F., Santini P., 2015, *ApJ*, 802, 137
- Coelho, P., & Gadotti, D. A. 2011, *ApJL*, 743, L13
- Comerón, S., Knapen, J. H., Beckman, J. E., et al. 2010, *MNRAS*, 402, 2462
- Côté, P., Piatek, S., Ferrarese, L., et al. 2006, *ApJS*, 165, 57
- Daddi, E., Renzini, A., Pirzkal, N. et al., 2005, *ApJ*, 626, 680
- de la rosa, I. G., et al. 2016, *MNRAS*, 457, 1916
- de Vaucouleurs, G. 1974, in *The Formation and Dynamics of Galaxies*, ed. J. R. Shakeshaft (Dordrecht: Reidel), *Proc. IAU Symp.*, 58, 1
- Dullo, B. T., & Graham, A. W. 2012, *ApJ*, 755, 163
- Dullo, B. T., & Graham, A. W. 2013, *ApJ*, 768, 36
- Dullo, B. T., & Graham, A. W. 2014, *MNRAS*, 444, 2700
- Ellison, S. L., Nair, P., Patton, D. R., et al. 2011, *MNRAS*, 416, 2182
- Eggen, O. J., Lynden-Bell, D., & Sandage, A. R. 1962, *ApJ*, 136, 748
- Eskridge, P. B., Frogel, J. A., Pogge, R. W., et al. 2000, *AJ*, 119, 536
- Erwin P., 2004, *A&A*, 415, 941
- Erwin, P., Saglia, R. P., Fabricius, M., et al. 2015, 446, 4039
- Erwin, P., & Sparke, L. S. 1999, *ApJ*, 512, L37
- Erwin, P., & Sparke, L. S. 2002, *AJ*, 124, 65
- Erwin P., & Sparke L. S., 2003, *ApJS*, 146, 299
- Ferrarese, L., Côté, P., Jordán, A., et al. 2006, *ApJS*, 164, 334
- Fisher, D. B., & Drory, N. 2008, *AJ*, 136, 773
- Friedli, D., Wozniak, H., Rieke, M., Martinet, L., & Bratschi, P. 1996, *A&AS*, 118, 461
- Fukugita, M., Shimasaku, K., & Ichikawa, T. 1995, *PASP*, 107, 945
- Gadotti, D. A., Seidel, M. K., Sánchez-Blázquez, P., et al. 2015, *A&A*, 584, A90
- Gallazzi, A., & Bell, E. F. 2009, *ApJS*, 185, 253
- Graham, A. W. 2013, in *Structure and Dynamics of Disk Galaxies*, Vol. 6, ed. T. D. Oswalt & W. C. Keel (Berlin: Springer), (arXiv:1108.0997)
- Graham, A. W. 2014, in *ASP Conf. Ser.* 480, *Structure and Dynamics of Disk Galaxies* ed. M. S. Seigar, & P. Treuthardt (San Francisco, CA: ASP), 185
- Graham, A. W., & Driver, S. P. 2005, *PASA*, 22, 118
- Graham, A. W., Dullo, B. T., Savorgnan, G. A. D., 2015, *ApJ*, 804, 32
- Graham A. W., Spitler L. R., 2009, *MNRAS*, 397, 2148
- Graham, A. W., & Worley, C. C. 2008, *MNRAS*, 388, 1708
- Heckman, T. M. 1980, *A&A*, 87, 152
- Ho, L. C., Filippenko, A. V., & Sargent, W. L. 1995, *ApJS*, 98, 477
- Ho, L. C., Filippenko, A. V., & Sargent, W. L. W. 1997b, *ApJS*, 112, 315
- Ho, L. C., Filippenko, A. V., & Sargent, W. L. W. 1997a, *ApJ*, 487, 591
- Jedrzejewski, R. I. 1987, *MNRAS*, 226, 747
- Jordi, K., Grebel, E. K., & Ammon, K. 2006, *A&A*, 460, 339
- Jungwiert, B., Combes, F., & Axon, D. J. 1997, *A&AS*, 125, 479
- KauAmann, G., Charlot, S., & White, S. D. M. 1996, *MNRAS*, 283, L117
- Kauffmann, G., Heckman, T. M., Tremonti, C., et al. 2003, *MNRAS*, 346, 1055
- Kewley, L. J., Groves, B., Kauffmann, G., & Heckman, T. 2006, *MNRAS*, 372, 961
- Kewley, L. J., Dopita, M. A., Leitherer, C., et al. 2013, *ApJ*, 774, 100
- Kewley, L. J., Dopita, M. A., Sutherland, R. S., Heisler, C. A., & Trevena, J. 2001, *ApJ*, 556, 121
- Knapen, J. H. 2005, *A&A*, 429, 141
- Knapen, J. H., Beckman, J. E., Heller, C. H., Shlosman, I., & de Jong, R. S. 1995, *ApJ*, 454, 623
- Knapen, J. H., Pérez-Ramírez, D., & Laine, S. 2002, *MNRAS*, 337, 808
- Knapen, J. H., Shlosman, I., & Peletier, R. F. 2000, *ApJ*, 529, 93
- Knapen J. H., Stedman S., Bramich D. M., Folkes S. L., Bradley T. R., 2004, *A&A*, 426, 1135
- Kormendy, J. 1982, *ApJ*, 257, 75
- Kormendy, J., & Bender, R. 2012, *ApJS*, 198, 2
- Kormendy, J., & Kennicutt, R. C., Jr. 2004, *ARA&A*, 42, 603
- Krajnović, D., Karick, A. M., Davies, R. L., et al. 2013, *MNRAS*, 433, 2812
- Laine, S., Shlosman, I., Knapen, J. H., & Peletier, R. F. 2002, *ApJ*, 567, 97
- Lauer, T. R., Faber, S. M., Gebhardt, K., et al. 2005, *AJ*, 129, 2138
- Laurikainen, E., Salo, H., & Buta, R. 2005, *MNRAS*, 362, 1319
- Laurikainen, E., Salo, H., Buta, R., Knapen, J. H., & Comerón, S. 2010, *MNRAS*, 405, 1089
- Martin, P. 1995, *AJ*, 109, 2428

- Moiseev, A. V., Valdés, J. R., & Chavushyan, V. H. 2004, *A&A*, 421, 433
- Mulchaey, J. S., Regan, M. W., & Kundu, A. 1997, *ApJS*, 110, 299
- Oh, S., Oh, K., & Yi, S. K. 2012, *ApJS*, 198, 40
- Paturel, G., Petit, C., Prugniel, P., et al. 2003, *A&A*, 412, 45
- Pfenniger, D., & Friedli, D. 1991, *A&A*, 252, 75
- Richings, A. J., Uttley, P., & Kröding, E. 2011, *MNRAS*, 415, 2158
- Sánchez-Gallego, J. R., Knapen, J. H., Wilson, C. D., et al. 2012, *MNRAS*, 422, 3208
- Scoville, N. Z., Matthews, K., Carico, D. P., & Sanders, D. B. 1988, *ApJ*, 327, L61
- Sellwood, J. A., & Wilkinson, A. 1993, *RPPh*, 56, 173
- Sérsic, J. L. 1968, *Atlas de Galaxias Australes* (Cordoba: Observatorio Astronómico)
- Shaw M., Axon D., Probst R., Gatley I., 1995, *MNRAS*, 274, 369
- Sheth, K., Vogel, S. N., Regan, M. W., Thornley, M. D., & Teuben, P. J. 2005, *ApJ*, 632, 217
- Shlosman, I., Begelman, M. C., & Frank, J. 1990, *Nature*, 345, 679
- Tonry, J. L., Dressler, A., Blakeslee, J., et al. 2001, *ApJ*, 546, 681
- Toomre, A., & Toomre, J. 1972, *ApJ*, 178, 623
- Worthey, G. 1994, *ApJS*, 95, 107
- Wozniak, H., Friedli, D., Martinet, L., Martin, P., & Bratschi, P. 1995, *A&A*, 111, 115